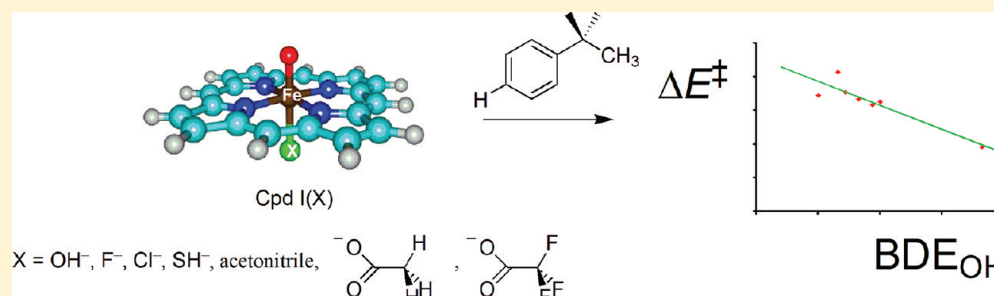


## Axial Ligand Effect On The Rate Constant of Aromatic Hydroxylation By Iron(IV)–Oxo Complexes Mimicking Cytochrome P450 Enzymes

Devesh Kumar,<sup>\*,†,‡</sup> G. Narahari Sastry,<sup>‡</sup> and Sam P. de Visser<sup>§</sup><sup>†</sup>Department of Applied Physics, School for Physical Sciences, Babasaheb Bhimrao Ambedkar University, Vidya Vihar, Rae Bareilly Road, Lucknow 226 025, India<sup>‡</sup>Molecular Modelling Group, Indian Institute of Chemical Technology, Hyderabad 500-607, India<sup>§</sup>Manchester Interdisciplinary Biocenter and School of Chemical Engineering and Analytical Science, University of Manchester, 131 Princess Street, Manchester M1 7DN, United Kingdom

S Supporting Information

## ABSTRACT:



The cytochromes P450 are important iron-heme based monooxygenases that catalyze a range of different oxygen atom transfer reactions in nature. One of the key bioprocesses catalyzed by these enzymes is the aromatic hydroxylation of unactivated arenes. To gain insight into axial ligand effects and, in particular, how it affects aromatic hydroxylation processes by P450 model complexes, we studied the effects of the axial ligand on spectroscopic parameters (trans-influence) as well as on aromatic hydroxylation kinetics (trans-effect) using a range of  $[Fe^{IV}(O)(Por^{+})X]$  oxidants with  $X = SH^-, Cl^-, F^-, OH^-,$  acetonitrile,  $GlyGlyCys^-, CH_3COO^-$ , and  $CF_3COO^-$ . These systems give red-shifted Fe–O vibrations that are dependent on the strength of the axial ligand. Despite structural changes, however, the electron affinities of these oxidants are very close in energy, but sharp differences in  $pK_a$  values are found. The aromatic hydroxylation of the para-position of ethylbenzene was tested with these oxidants, and they all show two-state-reactivity patterns although the initial low-spin C–O bond formation barrier is rate determining. We show, for the first time, that the rate determining barrier for aromatic hydroxylation is proportional to the strength of the O–H bond in the corresponding iron(IV)–hydroxo complex, i.e.,  $BDE_{OH}$ , hence this thermochemical property of the oxidant drives the reaction and represents the axial ligand effect. We have rationalized our observed barrier heights for these axially ligated systems using thermochemical cycles and a valence bond curve crossing diagram to explain the origins of the rate constants.

The cytochromes P450 (P450) are important enzymes found in most biosystems ranging from eukaryotes to prokaryotes. In humans they are mainly found in the liver, where they catalyze detoxification processes including the metabolism of drugs.<sup>1</sup> In addition, the P450s are known to be involved in biosynthetic pathways producing, for instance, hormones. Generally, the P450s react as monooxygenases that transfer one oxygen atom originating from molecular oxygen to a substrate, which is either hydroxylated (aliphatic or aromatic), epoxidized, or sulfoxidized.<sup>2</sup> Because of this large versatility in substrate activation, they are very important enzymes in biology but also biotechnological and pharmaceutical applications are being investigated.<sup>3</sup> Moreover, understanding their mechanism and function is important, but despite intense efforts in the field there still remain many questions to be answered.

Aromatic hydroxylation by P450 enzymes has always intrigued scientists, since a very strong C–H bond of an aromatic ring has to be broken. Despite this, the P450s seem to catalyze this reaction with relative ease. In biosystems, many important and vital processes include an aromatic hydroxylation step, and as such it contributes in biosynthesis and biodegradation of compounds. Thus, the metabolism of the hormone estrogen leads to the carcinogen 16- $\alpha$ -hydroxy-estrogen through an aromatic hydroxylation process and is catalyzed by liver P450 enzymes, whereby the P450 converts the hormone into a compound that can trigger breast cancer.<sup>4</sup> On the other hand, the aromatic hydroxylation of isoliquiritigenin by plant P450 enzymes gives a

Received: November 25, 2011

Published: December 01, 2011

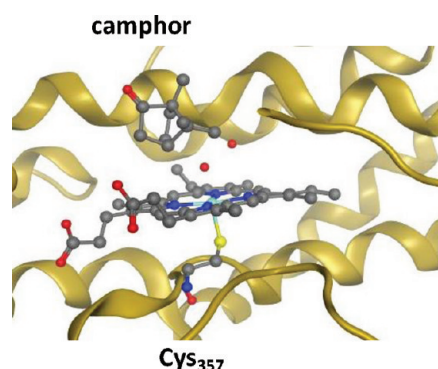


**Figure 1.** Active site structure of P450<sub>cam</sub> as taken from the 1DZ9 pdb file.<sup>16d</sup> Amino acids are labeled according to the pdb file.

product that has antitumor, antioxidant, and phytoestrogenic activity.<sup>5</sup> Aromatic hydroxylation reactions by the cytochromes P450 are also vital from a drug metabolism perspective. Examples of aromatic hydroxylation reactions of drug molecules by the P450s includes the para-hydroxylation of amphetamine and tamoxifen<sup>6</sup> as well as other substrates, such as, the  $\beta$ -blocker alprenolol<sup>7</sup> and the neurotoxin 1-methyl-4-phenyl-1,2,3,6-tetrahydropyridine that is a chemical inducer of Parkinson's disease.<sup>8</sup> The P450 isozyme CYP1B1 is particularly effective in catalyzing aromatic hydroxylation reactions and has been shown to hydroxylate, for instance, resveratrol, a cancer preventative agent found in red wine, and convert it into the anticancer agent piceatannol.<sup>9</sup> Finally, site-specific P450 mutants have been created that react regiospecifically by aromatic ring hydroxylation of substrates with the aim to create biotechnologically relevant P450s.<sup>10</sup>

Generally, the P450s utilize molecular oxygen on a heme center and convert it into an iron(IV)–oxo heme cation radical species  $[\text{Fe}^{\text{IV}}(\text{O})(\text{heme}^{+\bullet})]$  through a catalytic cycle that uses two electrons and two protons.<sup>2,11</sup> This iron(IV)–oxo heme cation radical species, which is also called Compound I (Cpd I), is the catalytic active species of P450 enzymes.<sup>2,12</sup> Until recently, this species was elusive and support for the assignment of Cpd I as active oxidant only came from indirect evidence, biomimetic and computational studies.<sup>13,14</sup> This was until Rittle and Green characterized Cpd I using Mössbauer, electron paramagnetic resonance, and UV–vis spectroscopic methods and found unambiguous proof for its activity in substrate hydroxylation.<sup>15</sup>

The active site of P450 enzymes includes an iron atom that is embedded into a heme (protoporphyrin IX) subunit, which is linked to the protein via a covalent linkage with a side chain of a cysteine residue via a thiolate bridge (Figure 1).<sup>16</sup> Other oxygen activating enzymes, such as peroxidases and catalases, by contrast, bind the heme to the protein via either a bridging histidine or tyrosinate ligand.<sup>17</sup> This difference in iron-ligand binding between the P450s on the one hand with peroxidases and catalases on the other hand, has been proposed to be the reason for their differences in catalytic function, whereby cysteine creates a “push-effect” and donates electrons to the heme center, while a histidine axial ligand withdraws electrons.<sup>18</sup> Indeed, a series of elegant biomimetic experiments of Gross et al.<sup>19</sup> and Nam et al.<sup>20</sup> have identified an axial ligand effect on substrate oxidation by iron(IV)–oxo oxidants with variable axial ligands. These studies used biomimetic iron-porphyrin oxidants where the ligand position trans to the oxo group was occupied by either an anion, e.g.,  $\text{F}^-$ ,  $\text{Cl}^-$ , acetate, perchlorate, etc., or a neutral

solvent molecule, e.g., acetonitrile. Thus, rate constants for styrene epoxidation and hydrogen abstraction reactions were measured and shown to vary with the nature of the axial ligand. Moreover, Nam et al.<sup>20b</sup> investigated the reactivities of  $[\text{Fe}^{\text{IV}}(\text{O})(\text{TPFP}^{+})\text{X}]$  with  $\text{TPFP} = \text{meso-tetrakis(pentafluoro-phenyl)porphyrinato}$  and  $\text{X} = \text{NCCH}_3$  or  $\text{Cl}^-$ . The reaction of  $[\text{Fe}^{\text{IV}}(\text{O})(\text{TPFP}^{+})\text{NCCH}_3]^+$  with ethylbenzene gave aromatic hydroxylation products, whereas the one using  $[\text{Fe}^{\text{IV}}(\text{O})(\text{TPFP}^{+})\text{Cl}]$  as an oxidant led to benzyl hydroxylation instead.

Understanding the catalytic mechanism of P450 enzymes is, therefore, important but sadly many fundamental details of the processes that take place are still unknown. In recent years, the technical details of hydrogen atom abstraction processes have been revealed through detailed valence bond (VB) curve crossing mechanisms.<sup>21</sup> More recent studies have also addressed the fundamental nature of double bond epoxidation,<sup>22</sup> dialkylsulfide sulfoxidation mechanisms,<sup>23</sup> as well as aromatic hydroxylation<sup>24</sup> by P450 enzymes. All these studies have in common that they investigate the reactivity of Cpd I of P450 with a systematic set of substrates. This indeed gives insight into the effects of the substrate on reactivity patterns. However, to gain insight into the effect of the oxidant on the reaction mechanisms, and in particular the choice of the axial ligand, we have performed a further set of calculations where we vary Cpd I but keep the substrate constant. The work described herein will generalize aromatic hydroxylation reactions by metal–oxo oxidants. Although aromatic hydroxylation reactions by P450 enzymes have been extensively studied by several groups,<sup>25–28</sup> the effect of the axial ligand remains elusive. Indeed, experimental studies identified a strong axial ligand effect upon aromatic hydroxylation reactions of arenes.<sup>20b</sup> Our previous studies on aliphatic hydroxylation by a range of Cpd I models established the role of the oxidant in reaction kinetics.<sup>29</sup> To gain insight into the axial ligand effect of aromatic hydroxylation and the implications on P450 catalysis, we have performed a density functional theory study. We show here that indeed the barrier heights and, consequently, the rate constants are affected by the choice of the axial ligand. In particular, we show here, for the first time, that using thermochemical properties of the oxidant and substrate the barrier height of the reaction and consequently the rate constant can be predicted for aromatic hydroxylation reactions.

## METHODS

The calculations described in this work use methods that have been thoroughly tested and benchmarked against experimental data.<sup>30</sup> The geometries were fully optimized with the *Jaguar* 7.7 and *Gaussian* 03 program packages, and a subsequent frequency calculation (at the same level of theory) confirmed the structures as local minima with real frequencies only or first order saddle points with a single imaginary frequency for the correct mode.<sup>31</sup> In order to compare the studies with related previous work, we chose the B3LYP hybrid density functional method for all calculations,<sup>32</sup> in combination with a Los Alamos type LACVP basis set on iron that includes a core potential coupled to 6-31G on the rest of the atoms (basis set B1).<sup>33</sup> Single point calculations were done using the triple- $\zeta$  quality LACV3P+ basis set on iron in combination with 6-311+G\* on the rest of the atoms (basis set B2) on the UB3LYP/B1 geometries on all structures described here. Test calculations that compared a potential energy landscape of a chemical reaction calculated with UB3LYP/B2 and UB3LYP/B2//UB3LYP/B1 showed only small changes in energy and geometry;<sup>22</sup>

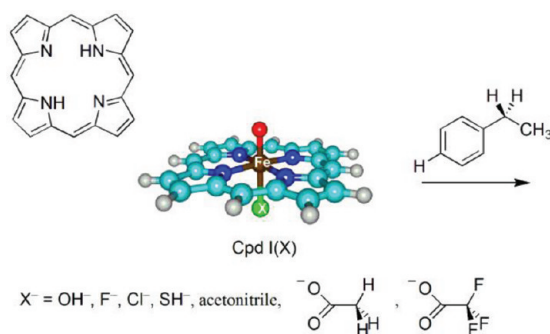


Figure 2. Oxidants and substrate used in this work.

therefore, the latter method was used here. Frequencies reported here were scaled with the recommended value of 0.9614.<sup>34</sup> All energies discussed in this work were obtained with UB3LYP/B2 and corrected with zero-point energy from the frequency calculations. To test the effect of the environment, we did single point calculations with the polarized continuum model with a dielectric constant of  $\epsilon = 5.7$  and probe radius of 2.7 Å mimicking a chlorobenzene solution and in-line with values found for enzymatic systems. These methods have been thoroughly tested, benchmarked, and shown, for instance, to reproduce experimental free energies of activation for these types of reactions within 3 kcal mol<sup>-1</sup> and give vibrational frequencies that are on average about 10–15 cm<sup>-1</sup> from experiments.<sup>35,36</sup>

To ascertain that the methods are not influenced by the density functional method chosen here, we ran a selection of single point calculations using OPBE<sup>37</sup> and B3LYP with 15% HF exchange (designated B3LYP\*).<sup>38</sup> These test calculations reproduced the B3LYP barrier heights within 2 kcal mol<sup>-1</sup> and gave similar trends, see the Supporting Information.

Cpd I was modeled as an iron(IV)–oxo embedded in protoporphyrin IX, whereby all side chains were abbreviated by hydrogen atoms. Previous work showed that replacing the heme side chains with hydrogen atoms gives little changes in the high-lying occupied and low-lying virtual orbitals of the chemical system, although some steric effects on substrate approach may occur.<sup>39</sup> We initially tested the description of the ligand system to mimic Cpd I of P450 by using an iron(IV)–oxo porphyrin cation radical model [Fe<sup>IV</sup>(O)(Por<sup>•+</sup>)X] with two types of axial ligands (X<sup>-</sup>): The first one uses thiolate and the second one a short peptide containing GlyGlyCys<sup>-</sup> that binds the metal via a thiolate bridge. The sets of geometry optimizations give similar geometries and group spin densities and charges. Moreover, it is shown that both the electron affinity of the oxidants and the BDE<sub>OH</sub> remain virtually the same for both ligand systems; therefore, we continued the reactivity profile with X = SH<sup>-</sup> as the P450 Cpd I. In a subsequent set of calculations we replaced the axial ligand (X<sup>-</sup>) in [Fe<sup>IV</sup>(O)(Por<sup>•+</sup>)X] with X = F<sup>-</sup>, Cl<sup>-</sup>, OH<sup>-</sup>, acetonitrile, CF<sub>3</sub>COO<sup>-</sup>, and CH<sub>3</sub>COO<sup>-</sup>. Because of two-state-reactivity patterns,<sup>40</sup> we calculated all reactions on the doublet and quartet spin state surfaces. Full details of all results are given in the Supporting Information document, while we focus on the main trends only.

## RESULTS

Here, the axial ligand effect on aromatic hydroxylation by iron(IV)–oxo porphyrin cation radical oxidants, which in the case of heme enzymes are known under the name Compound I

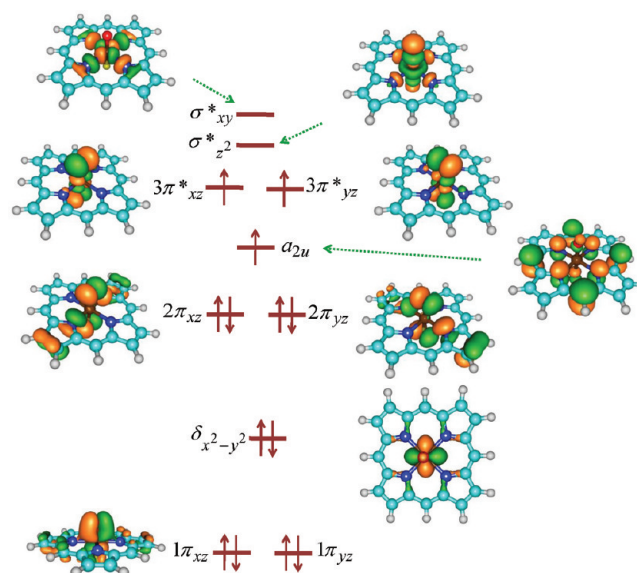


Figure 3. High-lying occupied and low-lying virtual orbitals of <sup>4</sup>Cpd I(F).

(Cpd I), is investigated. We varied the axial ligand (X) bound to the metal trans to the oxo group and with X = OH<sup>-</sup>, F<sup>-</sup>, Cl<sup>-</sup>, SH<sup>-</sup>, acetonitrile, acetate (CH<sub>3</sub>COO<sup>-</sup>), and trifluoroacetate (CF<sub>3</sub>COO<sup>-</sup>); Figure 2. This is a broad selection of ligand types with varying ligand effects and includes neutral (acetonitrile) as well as anionic axial ligands. As a model of aromatic hydroxylation reactions in general, we studied the aromatic hydroxylation on the para-position of ethylbenzene with DFT methods. To identify the type of Cpd I, we give the axial ligand in parentheses after Cpd I or in subscript after the label, while in superscript we give the overall spin multiplicity of the structure. For example, <sup>2</sup>Cpd I(F) is an iron(IV)–oxo porphyrin cation radical model of Cpd I with an axial fluoride ligand and in overall doublet spin state.

Before we will discuss the reactivity patterns of these iron(IV)–oxo porphyrin cation radical models, let us first highlight the electronic, geometric, and spectroscopic differences and comparisons between the various Cpd I complexes. Figure 3 gives the high-lying occupied and low-lying virtual orbitals of <sup>4</sup>Cpd I(F), where we focus on those orbitals that involve the metal 3d contributions plus a high lying  $\pi^*$ -type heme orbital. This labeling assumes that the z-axis is along the Fe–O bond and the x- and y-axes in between two Fe–N bonds of the porphyrin. As such, the metal 3d<sub>xz</sub> and 3d<sub>yz</sub> atomic orbitals interact with 2p<sub>x</sub>/2p<sub>y</sub> atomic orbitals on the oxo group as well as with those on the axial ligand. These orbitals form pairs of bonding (1 $\pi_{xz}$  and 1 $\pi_{yz}$ ), nonbonding (2 $\pi_{xz}$  and 2 $\pi_{yz}$ ), and antibonding (3 $\pi_{xz}^*$  and 3 $\pi_{yz}^*$ ) set of molecular orbitals. The bonding and nonbonding pairs of orbitals are all doubly occupied in Cpd I, but both  $\pi^*$  orbitals are singly occupied. These two unpaired electrons are either ferromagnetically or antiferromagnetically coupled to an unpaired electron in a mixed porphyrin-axial ligand type orbital designated a<sub>2u</sub> to give an overall quartet or doublet spin state, respectively. The a<sub>2u</sub> orbital mixes somewhat with the 2p<sub>z</sub> orbital on the axial ligand.<sup>41</sup> The remaining three 3d-type orbitals on the metal are the nonbonding  $\delta_{x^2-y^2}$  orbital that is in the plane of the porphyrin and two sets of  $\sigma/\sigma^*$  pair of orbitals. The  $\sigma_{z^2}$  and  $\sigma_{xy}$  orbitals (not shown in Figure 3) are low-lying and doubly occupied, while the  $\sigma^*$  orbitals ( $\sigma_{z^2}^*$  and  $\sigma_{xy}^*$ ) are virtual.

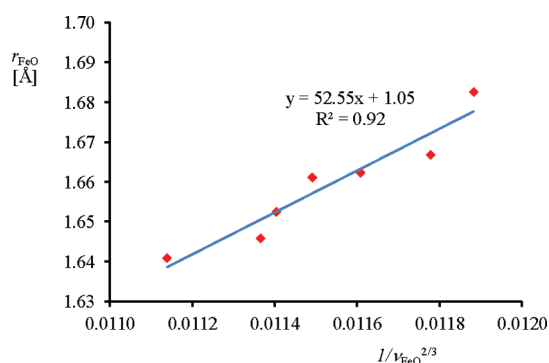


**Table 1.** Optimized Fe–O Bond Lengths ( $r_{\text{FeO}}$  in Å) of Cpd I(X) Structures in the Low-Spin (LS) and High-Spin (HS) Spin States<sup>a</sup>

Cpd I(L)	OH <sup>−</sup>	F <sup>−</sup>	Cl <sup>−</sup>	SH <sup>−</sup>	CH <sub>3</sub> COO <sup>−</sup>	CF <sub>3</sub> COO <sup>−</sup>	GlyGlyCys <sup>−</sup>
LS Data							
$r_{\text{FeO}}$ <sup>b</sup>	1.664	1.681	1.659	1.648	1.665	1.662	
$\nu_{\text{FeO}}$ <sup>c</sup>	783.2	786.1	821.3	837.2	793.8	802.5	
$\nu_{\text{FeX}}$ <sup>c</sup>	406.4	510.0	219.2	152.0	867.9	650.1	
HS Data							
$r_{\text{FeO}}$ <sup>b</sup>	1.691	1.683	1.661	1.652	1.667	1.662	1.641
$\nu_{\text{FeO}}$ <sup>c</sup>	696.6	772.0	811.9	821.2	782.3	799.6	850.7
$\nu_{\text{FeX}}$ <sup>c</sup>	407.2	513.7	224.2	161.9	868.6	650.2	259.6
EA(Cpd I) <sup>d</sup>	113.5	111.8	112.1	109.2	112.9	111.3	
BDE <sub>OH</sub> <sup>d</sup>	96.5	88.2	82.3	87.6	86.3	85.7	88.1

<sup>a</sup> Also given are vibrational frequencies ( $\nu_{\text{FeO}}$  and  $\nu_{\text{FeX}}$ ) for the Fe–O and Fe–X stretch vibration (in wavenumbers). <sup>b</sup> Values in Å. <sup>c</sup> Values in cm<sup>−1</sup>.

<sup>d</sup> Energies are in kcal mol<sup>−1</sup> relative to <sup>2</sup>Cpd I(X) and include ZPE and solvent corrections.

**Figure 4.** Badger plot for the Fe–O bond length versus  $1/\nu_{\text{FeO}}^{2/3}$  with  $\nu_{\text{FeO}}$  the stretch vibration for the Fe–O bond for the series of Cpd I species of Figure 2 plus Cpd I(NCCH<sub>3</sub>). Data for high-spin Cpd I(X) structures were used.

The  $\sigma_{z^*}$  orbital reflects the antibonding  $\sigma$ -interaction of the metal with the distal and axial ligands, whereas the  $\sigma_{xy}^*$  orbital is orthogonal to the  $\sigma_{z^*}$  orbital and interacts in the plane of the porphyrin with  $\sigma$ -orbitals on the four pyrrole nitrogen atoms. The  $\sigma_{xy}^*$  orbital is high in energy and remains virtual during the complete reaction mechanism. The  $\delta_{x^2-y^2}$  orbital is also located in this plane but due to the symmetry of the porphyrin ring cannot form bonding and antibonding pairs and hence is a nonbonding orbital.

Gross and co-workers showed that the axial ligand displays a trans-influence due to changes in the spectroscopic parameters of complexes with different axial ligands as well as a trans-effect on the reactivity patterns.<sup>19</sup> Therefore, we first did an in-depth analysis of the structures and spectroscopic parameters of the Cpd I models shown in Figure 2 together with an elaborate P450 Cpd I model, where the axial ligand is described by a small chain of amino acids containing GlyGlyCys<sup>−</sup>: Cpd I(GlyGlyCys). Thus, this model includes the amide–sulfur hydrogen bonding interactions on the axial ligand site that are known to be important in regulating the electronic properties of Cpd I, i.e. through a push effect of the thiolate ligand, and consequently the reactivity patterns.<sup>42</sup> In all cases we find the quartet and doublet spin state structures within 1 kcal mol<sup>−1</sup>, but the quartet spin state is slightly lower in energy. This is in agreement with EPR

studies on oxo–iron porphyrin cation radical models of Gross, which implicated these structures as high-spin states.<sup>19b</sup> Optimized Fe–O bond lengths are given in Table 1 as well as vibrational stretch frequencies for the Fe–O and Fe–X modes.

The Fe–O distances range from 1.641 Å for <sup>4</sup>Cpd I-(GlyGlyCys) to 1.691 Å for <sup>4</sup>Cpd I(OH), which implies that a difference of 0.05 Å has occurred due to the change in axial ligand bound trans to the iron(IV)–oxo bond. Although this is a minor change from a mechanistic point of view, it causes a significant effect on the spectroscopic parameters for these Cpd I species. In particular, a difference in Fe–O bond strength should influence the Fe–O vibrational frequency. Indeed, our calculated Fe–O vibrational frequencies in the quartet spin state range from 696.6 cm<sup>−1</sup> for <sup>4</sup>Cpd I(OH) to 850.7 cm<sup>−1</sup> for <sup>4</sup>Cpd I-(GlyGlyCys), whereby a long Fe–O distance corresponds to the lowest Fe–O stretch vibration and a short Fe–O distances with high vibrational modes. Thus, the experimentally determined value of  $\nu_{\text{FeO}}$  for [Fe<sup>IV</sup>(O)(TMP<sup>+</sup>)X], X = F<sup>−</sup>/Cl<sup>−</sup> and TMP = tetramesitylporphyrin,<sup>19b</sup> is 801 cm<sup>−1</sup>. Our calculated value of <sup>4</sup>Cpd I(Cl) is within 10 cm<sup>−1</sup> of this; however, the calculations predict a strong deviation in Fe–O stretch vibration between Cpd I(F) and Cpd I(Cl) that was not found experimentally. This may be due to the fact that our calculated model lacks meso-substituents and/or was optimized in the gas-phase.

Badger<sup>43</sup> proposed a correlation between the Fe–O bond strength ( $r_{\text{FeO}}$ ) and the strength of the stretch vibration ( $\nu_{\text{FeO}}$ ) for this bond (eq 1), via two constants  $c_{ij}$  and  $d_{ij}$ . Green showed that this equation successfully predicts the Fe–O bond strength in peroxidases and P450 Cpd I species.<sup>44</sup> To find out whether the equation also applies to our series of axially ligated Cpd I mimics, we determined the Fe–O stretch vibrations and plotted those against the Fe–O bond length in Figure 4. As can be seen from Figure 4, the trend is linear and indeed Badger's rule applies to axially ligated iron(IV)–oxo porphyrin cation radical systems. Note here that the trend includes neutral (acetonitrile) as well as anionic axial ligands.

$$r_{\text{FeO}} = \frac{c_{ij}}{(\nu_{\text{FeO}})^{2/3}} + d_{ij} \quad (1)$$

To understand the changes in vibrational frequencies upon changing the axial ligand, we did an in-depth analysis of the

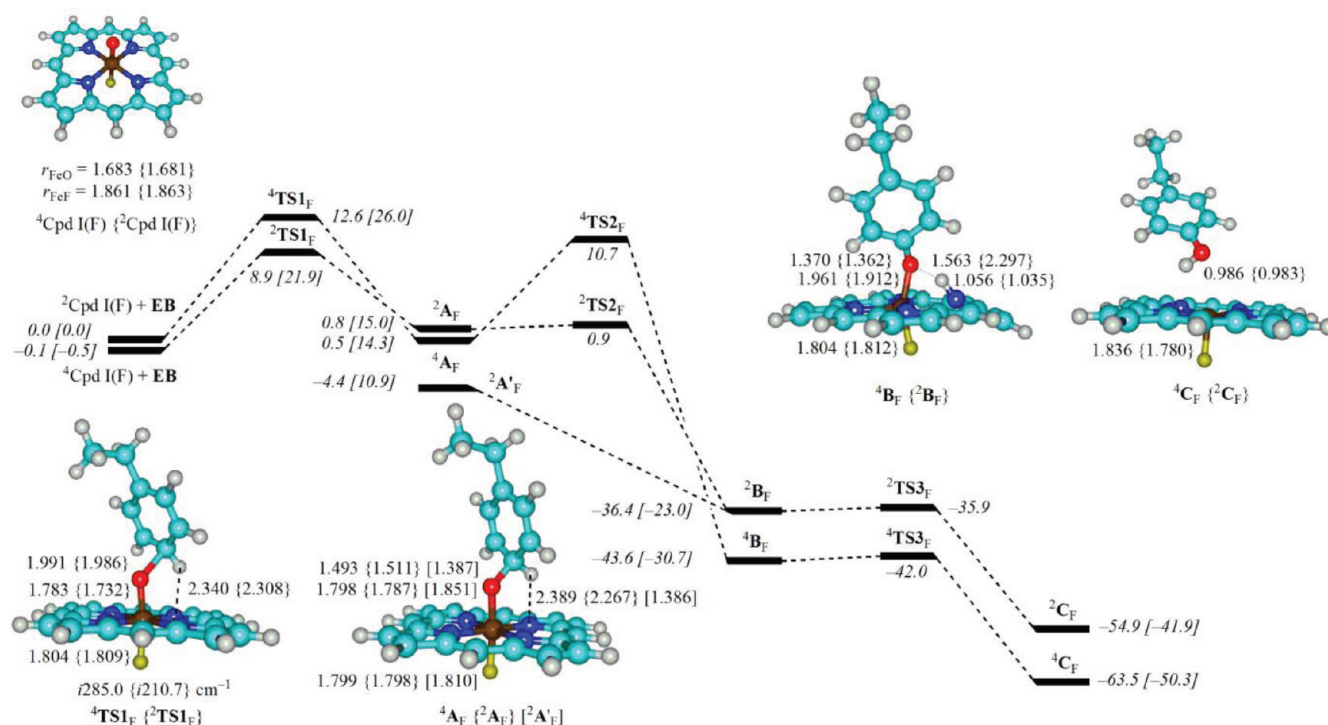
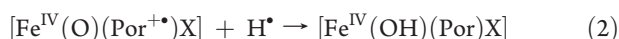


**Figure 5.** Potential energy surface of aromatic hydroxylation of ethylbenzene by Cpd I(F) as calculated with DFT methods. All energies are in kilocalories mole<sup>-1</sup> relative to isolated reactants in the quartet spin state. Also shown are optimized geometries of critical points with bond lengths in angstroms and the imaginary frequency in the transition states in wave numbers. The energies are calculated at the UB3LYP/BS2//UB3LYP/BS1 level of theory and contain zero point corrections, while values in square brackets are free energies.

different Cpd I species with the aim to elucidate the quantum chemical origins of these differences. Thus, we calculated the electron affinity (EA) and hydrogen atom abstraction ability (bond dissociation energy, BDE<sub>OH</sub>) of each Cpd I structure. BDE<sub>OH</sub> is defined as the negative of the enthalpy change for reaction 2 and can be written in terms of a separate electron and proton abstraction, eq 3.



$$\text{BDE}_{\text{OH}} = \text{EA} + 2.303RT \text{p}K_{\text{a}} + 54.9 \text{ kcal mol}^{-1} \quad (3)$$

The EA values in Table 1 give a spread of only 4.3 kcal mol<sup>-1</sup> for the various Cpd I species; therefore, the axial ligand hardly affects the reduction potential of Cpd I. Electron abstraction by these Cpd I models, in all cases, fills the porphyrin-type  $a_{2u}$  orbital with a second electron. This orbital is a pure porphyrin based orbital for Cpd I(F), Cpd I(CH<sub>3</sub>COO), and Cpd I(CF<sub>3</sub>COO) but contains significant mixing with a  $2p_z$  orbital on the axial ligand in Cpd I(OH) and Cpd I(SH). The latter two structures, in the gas-phase, give spin densities of -0.71 and -0.50 on the porphyrin ring and -0.36 and -0.60 on the axial ligand, respectively. Because of this, the latter two structures have the highest and lowest EA values. The amount of mixing between the  $a_{2u}$  and  $3p_z$  (thiolate) orbitals was shown to be dependent on hydrogen bonding donor groups, and a QM/MM approach reduced the amount of radical character on the thiolate of Cpd I dramatically.<sup>45</sup> Calculations on small model complexes showed a large effect on the electronic properties of Cpd I(SH) due to hydrogen bonding interactions but very little influence on hydrogen abstraction reactions.<sup>46</sup> In agreement with that, the data in Table 1 shows a negligible effect of hydrogen bonding on

BDE<sub>OH</sub> so that the hydrogen abstraction ability of Cpd I(SH) and Cpd I(GlyGlyCys) is expected to be the same.

The BDE<sub>OH</sub> values vary from 81.3 kcal mol<sup>-1</sup> for Cpd I-(NCCH<sub>3</sub>) to 96.5 kcal mol<sup>-1</sup> for Cpd I(OH) and, hence, cover a range of more than 15 kcal mol<sup>-1</sup>. Thermodynamically, BDE<sub>OH</sub> can be described as the sum of an electron and a proton transfer and is split into an EA and pK<sub>a</sub> term as shown in eq 3, with  $R$  the gas constant and  $T$  the temperature.<sup>47</sup> The constant of 54.9 kcal mol<sup>-1</sup> in eq 3 represents the ionization potential of a hydrogen atom and solvent corrections to the equation. As follows from the data in Table 1, the EA values are virtually independent of the axial ligand and fairly constant. The change in BDE<sub>OH</sub> along the axial ligand series, therefore, correlates with a change in the pK<sub>a</sub> value of the oxidant. This is in agreement with experimental studies of Green and Goldberg that came to the same conclusion.<sup>16c,48</sup>

Table 1 also gives the values of the Fe–X stretch vibrations as taken from the Gaussian frequency calculations. Thus, very strong differences in Fe–axial ligand frequencies are found that range from 152.0 cm<sup>-1</sup> for the Fe–S stretch vibration in <sup>2</sup>Cpd I(SH) to 868.6 cm<sup>-1</sup> for the Fe–OOCCH<sub>3</sub> stretch vibration in <sup>4</sup>Cpd I(CH<sub>3</sub>COO). In contrast to the iron(IV)–oxo frequencies, therefore, the Fe–X vibrations do not seem to be proportional to the strength of the Fe–X bond. At first glance a higher vibrational frequency for Fe–OOCCH<sub>3</sub> than Fe=O may look odd, but experimental <sup>16</sup>O<sub>2</sub>/<sup>18</sup>O<sub>2</sub> studies on the iron(IV)–oxo-(carboxylato) species of taurine/α-ketoglutarate dioxygenase (TauD) found similar vibrational frequencies as those reported here.<sup>49</sup> The difference spectrum showed isotope sensitive peaks at 821 and 859 cm<sup>-1</sup>, whereby the lower one was identified as the Fe=O vibration, while the latter was shown to be an Fe–carboxylate vibration.

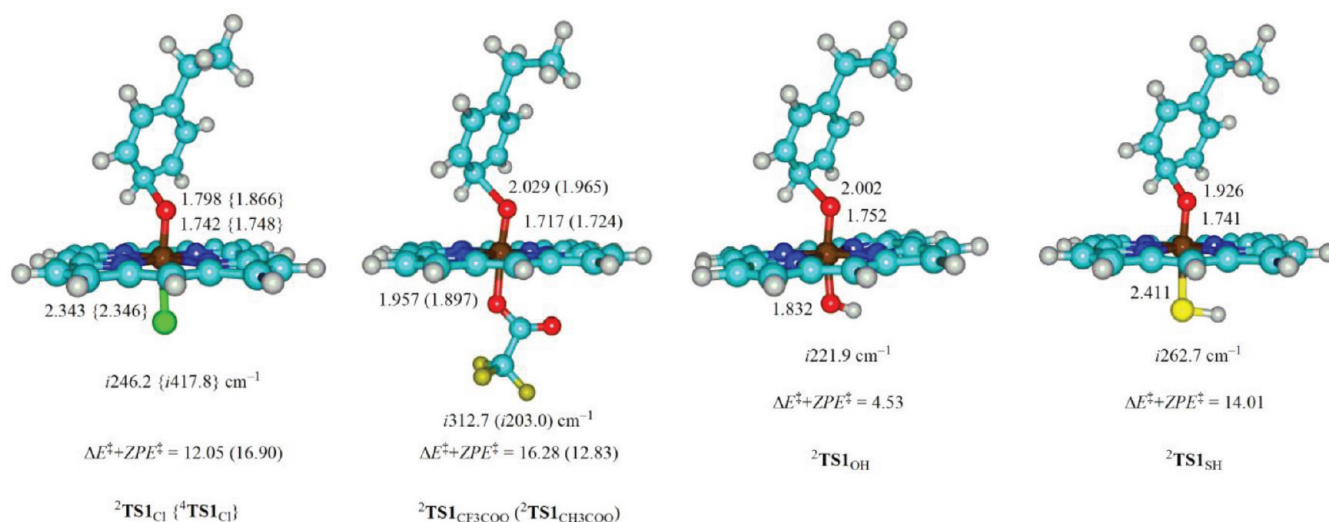


**Figure 6.** Optimized geometries of rate determining transition states **TS1** from the reaction of ethylbenzene with Cpd I(X), X = Cl<sup>−</sup>, CF<sub>3</sub>COO<sup>−</sup>, CH<sub>3</sub>COO<sup>−</sup>, OH<sup>−</sup>, and SH<sup>−</sup>. Geometries optimized at UB3LYP/B1 with bond lengths given in angstroms and the imaginary frequency in the transition state in wavenumbers.

Our axial carboxylate system gives vibrational frequencies for the Fe–OOCCH<sub>3</sub> that are very close to these values.

Subsequently, we investigated the aromatic hydroxylation of ethylbenzene (EB) by the selection of Cpd I models with varying axial ligands. As an example, we give in Figure 5 the aromatic hydroxylation mechanism of ethylbenzene by Cpd I(F). All other oxidants give similar potential energy profiles and the only difference arises from the relative energies. The aromatic hydroxylation mechanism found here is similar to those reported before for P450 model complexes, although different substrates were used.<sup>26,27</sup> The reaction starts with an electrophilic attack of the oxo group on the carbon atom in the para-position from ethylbenzene to give a Meisenheimer complex (**A**) via an electrophilic transition state **TS1**. In this complex, the aromaticity of the benzene ring is distorted and as a consequence its basicity is very large. Structure **A** either has a radical on the aromatic ring or a cation on the aromatic ring (in **A'**). The ipso-proton is shuttled to one of the nitrogen atoms of the porphyrin ring via a barrier **TS2** to form the proton transfer intermediate **B**. During this process, the aromaticity is put back into the aromatic ring and **B**, therefore, can be regarded as a phenolate bound to an iron(III) ion inside a protonated porphyrin. Because of the protonation of one of its pyrrole groups, the porphyrin ring in structure **B** is not planar but significantly distorted, where the protonated pyrrole ring is tilted out of the plane through the other nitrogen atoms. In a final step, the proton is relayed to the phenolate to give para-hydroxyethylbenzene products (**C**) via a transition state **TS3**. This brings the porphyrin ring back to planarity and removes the temporary tilt that is characteristic for structure **B**. Note that an early report of Siegbahn and co-workers on a nonheme metal–oxo oxidant found a direct hydrogen atom migration rather than the proton-shuttle mechanism found for iron–porphyrin systems.<sup>50</sup> Detailed DFT studies that compared the two mechanisms, however, found the proton-shuttle mechanism to be significantly lower in energy;<sup>26a</sup> hence, we focus on that mechanism here only.

As follows from Figure 5, the first step in this mechanism is the rate determining step with a barrier of 8.9 kcal mol<sup>−1</sup> on the low-spin surface and 12.6 kcal mol<sup>−1</sup> on the high-spin surface. This difference in barrier between the low- and high-spin surfaces was

explained by the differences in electron transfer that take place in an electrophilic attack.<sup>26</sup> After passing the barrier (<sup>4,2</sup>**TS1**) the system relaxes to the radical intermediates (<sup>4,2</sup>**A**), which have an electronic configuration that resembles the transition state structures closely. The overall reaction energy (driving force) for the formation of radical intermediates is almost thermo-neutral. There is, however, a slightly more stable intermediate, namely, the cationic intermediate (**A'**), although, it is a first-order saddle point with an imaginary frequency of i630.5 cm<sup>−1</sup> for the proton transfer from the ipso-position to the nearest nitrogen atom of the porphyrin ring. By contrast, the radical intermediates (<sup>4,2</sup>**A**) are genuine local minima, although the subsequent proton transfer mechanism via **TS2** is virtually barrierless on the low-spin surface while it encounters a somewhat larger barrier in the high-spin surface. Previous computational studies<sup>26,27</sup> also calculated the cationic intermediate (**A'**) below the radical intermediates <sup>4,2</sup>**A** by several kilocalories mole<sup>−1</sup>. However, the relative energies between the radical and cationic intermediates and the degree of charge-transfer in the transition state were found to be dependent on the substrate.<sup>24</sup> Moreover, in previous work the rate determining barriers had strong cationic character, whereas here **TS1** is a radical, later we will give an in-depth discussion on these differences.

The reaction leading to complexes **C** is highly exothermic due to the fact that the aromaticity is put back into the arene ring and the proton transfer gives a phenolate anion bound to an iron(III) center. The protonated heme structure (**C**) has a twisted pyrrole ring and can relay its proton back to the phenolate to form phenol products. QM/MM studies<sup>27c</sup> showed that there is sufficient space in the heme binding pocket to accommodate for these structural changes. Nevertheless, the barriers leading to products are very small (<2 kcal mol<sup>−1</sup>), so the last step will proceed very fast. In the past, we showed that structure **C** in the benzene hydroxylation mechanism of P450 is also an intermediate en route to cyclohexadienone products through proton relay to the ortho-carbon atom.<sup>26a</sup> However, the barrier leading to cyclohexadienone products was found to be significantly higher in energy than the one giving phenol products; therefore, we will not focus on this alternative mechanism here.



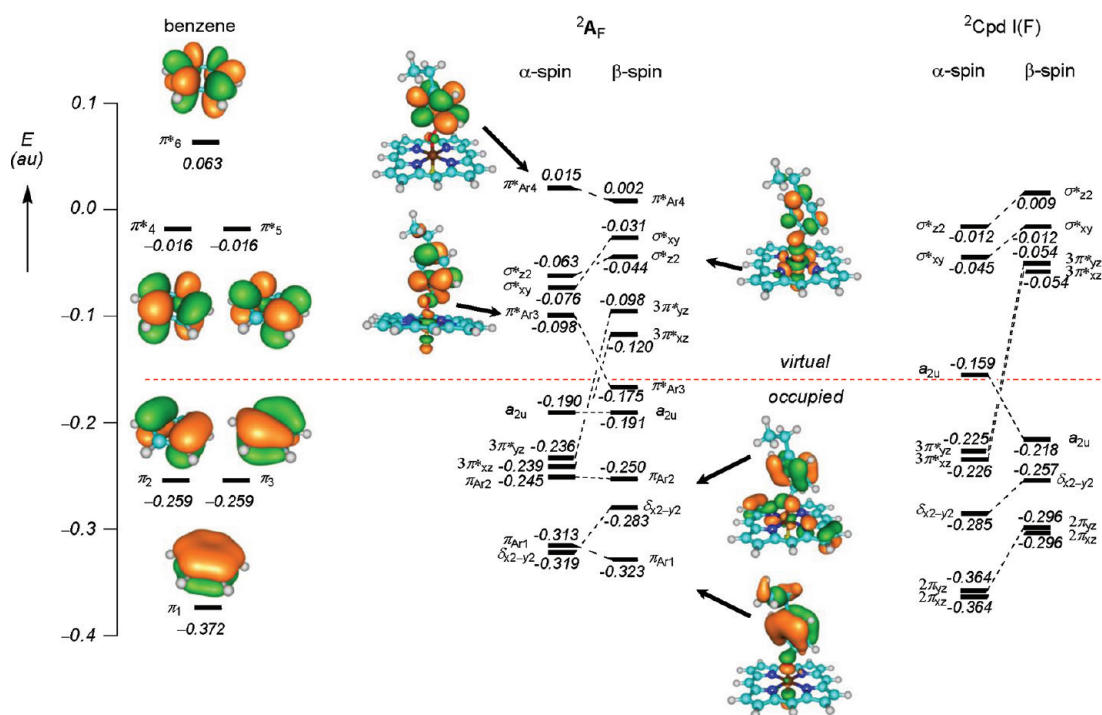


**Figure 7.** Orbital diagram of benzene (left-hand-side),  $^2A_F$  (middle), and  $^2Cpd\ I(F)$  (right-hand-side). Orbital energies taken from UB3LYP/B2//UB3LYP/B1 calculations.

A series of density functional theory studies on iron(IV)–oxo porphyrins identified a large axial ligand effect on the kinetics of substrate activation by substrates, whereby neutral ligands such as imidazole (mimicking peroxidases) gave substantial differences in reactivity patterns over anionic ligands like thiolate or phenolate (mimicking catalase).<sup>51</sup> To this end, we investigated the axial ligand effect on aromatic hydroxylation reactions and optimized the geometries of all rate determining transition states which are given in Figure 6. The geometries are typical for an electrophilic attack of an iron(IV)–oxo on an aromatic ring and all optimized geometries give structures that are very similar. Despite this, there are remarkable differences in C–O activation barrier height (TS1) of ethylbenzene by Cpd I models that on the low-spin surface range from 4.5 kcal mol<sup>−1</sup> for Cpd I(OH) to 16.3 kcal mol<sup>−1</sup> for Cpd I(CF<sub>3</sub>COO). The difference in barrier height between these two processes should correlate with a considerable rate enhancement for the aromatic hydroxylation reaction ( $k_{OH}/k_{CF_3COO}$ ) of several orders of magnitude. Similar trends are observed for the driving force of the reaction, i.e., the energy between reactants and  $^2A$  (Supporting Information). Therefore, the axial ligand effect manifests itself by changing the driving force and kinetics of the aromatic hydroxylation reaction.

Attempts to find a correlation between either the Fe–O distance and/or the C–O distance with the barrier height gave no linear correlation (Supporting Information). The imaginary frequencies in the transition states range from  $i203.0\text{ cm}^{-1}$  for  $^2TS1_{CF_3COO}$  to  $i312.7\text{ cm}^{-1}$  for  $^2TS1_{CH_3COO}$  and compare well to values found before for aromatic hydroxylation reactions.<sup>26–28</sup> Note that all transition states are characterized via a side-on approach of the substrate on the iron(IV)–oxo group, where the ipso-hydrogen atom forms a hydrogen bonding interaction with one of the nitrogen atoms of the porphyrin ring. In the case of

Cpd I(SH), we also calculated a face-on transition state, where the aromatic ring of the substrate is parallel to the porphyrin ring (Supporting Information Figure S20). In analogy to previous work,<sup>27c</sup> however, the face-on approach has a barrier that is a several kilocalories mole<sup>−1</sup> higher in energy than the side-on TS, i.e., 17.1 versus 14.0 kcal mol<sup>−1</sup>.

## DISCUSSION

So what is the origin of the axial ligand effect and what are the intrinsic properties of the reactant and/or substrate that determine the barrier heights/rate constants for aromatic hydroxylation? In the following sections, we will try to give an in-depth understanding of the fundamental properties that lead to the dramatic differences in aromatic hydroxylation rate constant by these Cpd I mimics with varying axial ligands.

To understand the electron transfer process that takes place for the conversion from  $^2Cpd\ I$  to  $^2A$  via the transition state  $^2TS1$ , consider in Figure 7 the orbital energy levels of the two reactants (outer left- and right-hand-side of Figure 7) and those for  $^2A_F$  for the system with fluoride axial ligand, where we use benzene as the aromatic substrate for simplicity. All other chemical systems discussed here follow the same principles. Thus, a substrate with an aromatic ring, such as benzene, will have a set of six  $\pi/\pi^*$ -orbitals of which the lowest three are doubly occupied ( $\pi_1$ ,  $\pi_2$  and  $\pi_3$ ); the latter two are degenerate. Higher in energy are the virtual  $\pi^*$  orbitals on the aromatic ring ( $\pi_4^*$ ,  $\pi_5^*$ , and  $\pi_6^*$ ). As discussed above,  $^2Cpd\ I(F)$  has orbital occupation (core)  $1\pi_{xz}^2 1\pi_{yz}^2 2\pi_{xz}^2 2\pi_{yz}^2 \delta_{x^2-y^2}^2 3\pi_{xz}^* 3\pi_{yz}^* a_{2u}^1$ , whereby the unpaired electrons in the  $\pi^*$  orbitals are antiferromagnetically coupled to the  $a_{2u}$  electron.

Electrophilic attack of the iron(IV)–oxo group on one of the carbon atoms of the aromatic ring leads to a C–O bond formation and distortion of the aromatic ring from planarity. Consequently,

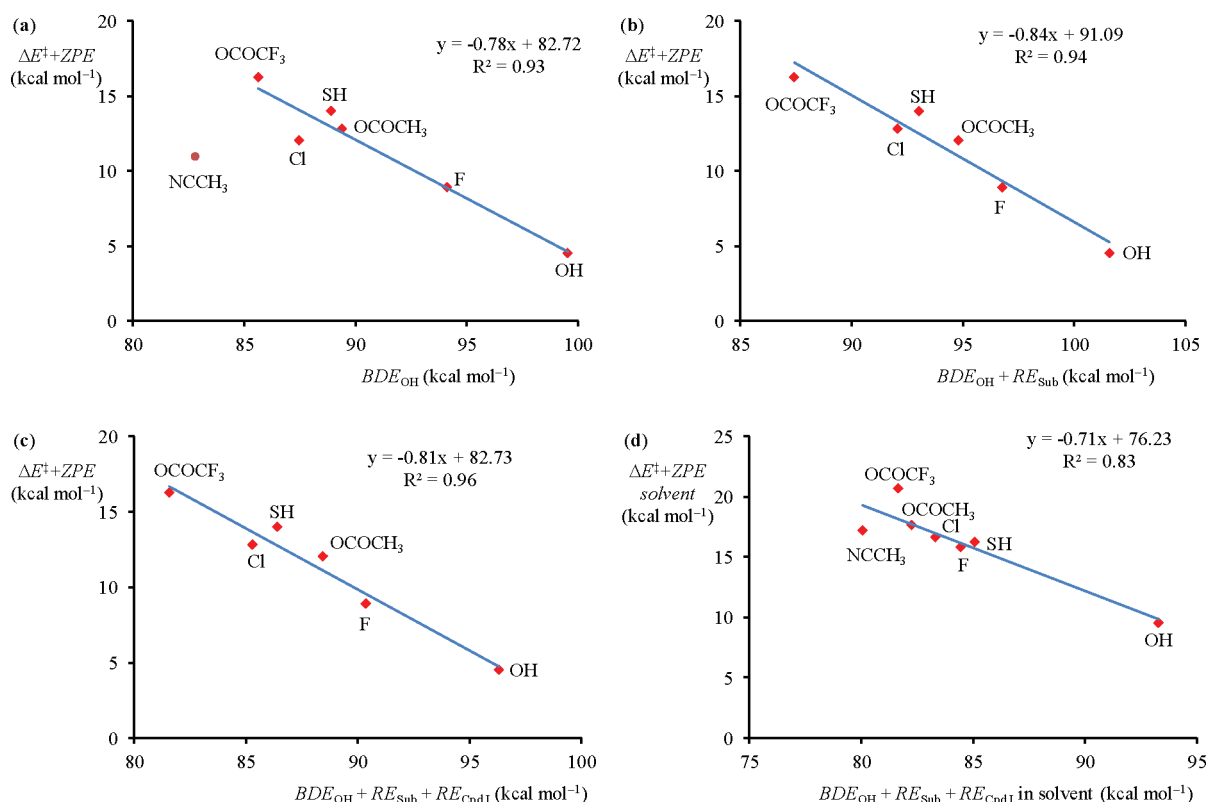
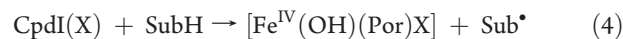


**Figure 8.** Correlation between aromatic hydroxylation barrier height and  $\text{BDE}_{\text{OH}}$  value. Data for low-spin structures only.

the aromatic ring of the substrate in  $^2\text{A}$  has a conjugated  $\pi$ -system spread out over only five of its carbon atoms. This has a major effect on the orbital energy levels as can be seen from the middle panel in Figure 7. The lowest aromatic ring orbital ( $\pi_{\text{Ar1}}$ ) is raised from  $-0.372$  au in isolated benzene to  $-0.313$  ( $\alpha$ ) and  $-0.323$  ( $\beta$ ) au in  $^2\text{A}_\text{F}$  due to decreased  $\pi$ -conjugation. Not all substrate  $\pi$ -type orbitals change as much in energy as  $\pi_{\text{Ar1}}$ . For instance, the  $\pi_2$  orbital in benzene does not have orbital occupation on the carbon atom that binds oxygen in  $^2\text{A}$ , hence the corresponding  $\pi_{\text{Ar2}}$  orbital energy level is close to that of  $\pi_2$  in isolated benzene. The  $\pi_3$  orbital of benzene is significantly raised in energy after oxygen binds to the ipso-carbon atom and splits into a virtual  $\pi_{\text{Ar3}}^*$   $\alpha$ -orbital and an occupied  $\beta$ -orbital. Its reactant electron is transferred into the vacant  $a_{2u}$  orbital to create a radical intermediate with configuration  $\pi_{\text{Ar1}}^2 \pi_{\text{Ar2}}^2 \delta_{x^2-y^2}^2 3\pi_{xz}^{*1} 3\pi_{yz}^{*1} a_{2u}^2 \pi_{\text{Ar3}}^{*1}$ . Note as well the mixing of  $\pi_{\text{Ar3}}^*$  with the  $\sigma_{z^2}^*$  orbital along the axial ligand–Fe–O axis. Obviously, the larger the contribution of the axial ligand effect into the  $\sigma_{z^2}^*$  orbital is, the stronger the effect on the energy level of this mixed  $\pi_{\text{Ar3}}^* - \sigma_{z^2}^*$  orbital will be the case. This will affect the electron transfer possibility during the C–O bond formation step. Electron transfer from the  $\beta$ -occupied  $\pi_{\text{Ar3}}^*$  orbital in  $^2\text{A}_\text{F}$  to the vacant  $3\pi_{xz}^*$  converts  $^2\text{A}_\text{F}$  into the lowering lying  $^2\text{A}'_\text{F}$ . Thus, the orbital occupation shows favorable side-on approach that results in stabilization due to mixing of the  $\pi_{\text{Ar3}}^*$  and  $\sigma_{z^2}^*$  molecular orbitals. This is in agreement to the lowering of the barrier height as compared to a face-on transition state (Supporting Information). Further stabilization of the side-on structure is as a result of a hydrogen bonding interaction between the ipso-proton and one of the nitrogen atoms of the porphyrin ring.

Let us in the following focus on the thermodynamics of the electrophilic reaction mechanism and try to find a correlation that will enable us to make predictions of rate constants of

aromatic hydroxylation processes. Thus, in an aliphatic hydroxylation reaction between Cpd I(X) and a substrate (SubH), the reaction enthalpy of a hydrogen atom abstraction ( $\Delta H_{\text{HA}}$ ) can be described by the differences in bond dissociation energy (BDE) of the aliphatic C–H bond that is broken ( $\text{BDE}_{\text{CH}}$ ) and the strength of the O–H bond that is formed ( $\text{BDE}_{\text{OH}}$ ), eqs 4–6.<sup>47</sup> Many experimental and computational studies confirmed a correlation between rate constant and  $\text{BDE}_{\text{CH}}$  for a series of hydrogen atom abstraction reactions.<sup>52,53</sup>



$$\Delta H_{\text{HA}}(\text{eq2}) = \text{BDE}_{\text{CH}} - \text{BDE}_{\text{OH}} \quad (5)$$



In an aromatic hydroxylation reaction, by contrast, a C–O rather than a H–O bond is formed. However, recent studies on trends in substrate epoxidation reactions by a range of Cpd I oxidants showed that the formation of the C–O bond in this mechanism can be approximated by the formation of a H–O bond. Therefore, a plot of the epoxidation barrier height against  $\text{BDE}_{\text{OH}}$  for the reaction of propene with Cpd I(X) gave a linear correlation.<sup>22</sup> In a similar vein, a correlation between sulfoxidation barrier height and  $\text{BDE}_{\text{OH}}$  was found to be linear, so that  $\text{BDE}_{\text{OH}}$  appears to be a good representation of a C–O as well as an S–O bond formation step.<sup>54</sup> To find out whether the same applies to aromatic hydroxylation, we plot in Figure 8 the aromatic hydroxylation barriers versus  $\text{BDE}_{\text{OH}}$  for the reaction of ethylbenzene with Cpd I(X),  $\text{X} = \text{F}^-$ ,  $\text{Cl}^-$ ,  $\text{SH}^-$ ,  $\text{OH}^-$ , acetonitrile,  $\text{CH}_3\text{COO}^-$ , and  $\text{CF}_3\text{COO}^-$ .



If we exclude acetonitrile from the correlation and focus on the Cp<sub>d</sub> I oxidants with anionic ligands only, then the correlation is good and an  $R^2$  value of 0.93 is found. Following previous studies in the field,<sup>21</sup> we also calculated the reorganization energy (RE) of both the substrate (RE<sub>Sub</sub>) and the oxidant (RE<sub>Cpd I</sub>) in the transition states. The values of RE<sub>Sub</sub> were calculated from the energies obtained from the substrate geometry in the transition state minus that for the fully relaxed structure. Similarly, the RE<sub>Cpd I</sub> values were calculated from the difference in energy between the structure of Cp<sub>d</sub> I in the transition state geometry minus that for the fully relaxed geometry. Correcting the BDE<sub>OH</sub> values for RE<sub>Sub</sub> gives a small improvement of the correlation with barrier height (Figure 8b). Further corrections with RE<sub>Cpd I</sub> gives an even better  $R^2$  value of 0.96 for the relationship with barrier height (Figure 8c). Consequently, the barrier heights of aromatic hydroxylation by iron(IV)–oxo porphyrin cation radical systems are proportional to BDE<sub>OH</sub>. This implies that barrier heights of substrates can be predicted using known values of BDE<sub>OH</sub> of the oxidants used.

The series of oxidants discussed so far all have in common that the axial ligands used are anionic. To find out whether Cp<sub>d</sub> I species with a neutral ligand will also fit the trend, we did a further

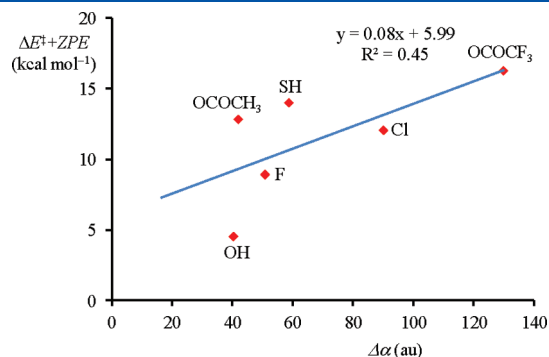


**Figure 9.** Correlation between aromatic hydroxylation barrier height and reaction polarizability for the low-spin reactions by Cp<sub>d</sub> I(X), X = OH<sup>-</sup>, F<sup>-</sup>, Cl<sup>-</sup>, SH<sup>-</sup>, acetate, and CF<sub>3</sub>COO<sup>-</sup>.

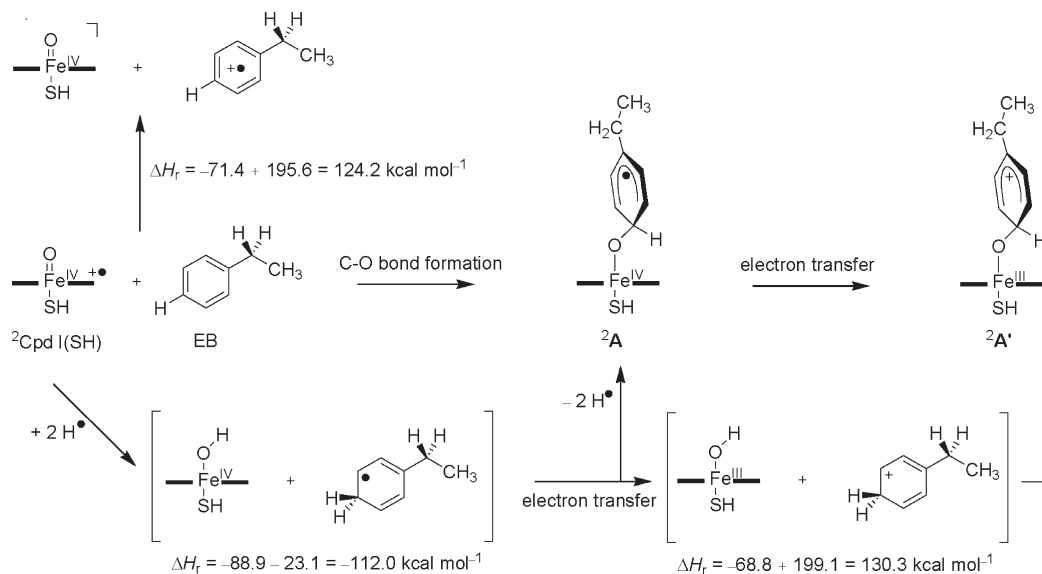
set of calculations using Cp<sub>d</sub> I(NCCH<sub>3</sub>) as an oxidant and overall charge 1+. As follows from Figure 8a, the barrier height of <sup>2</sup>TS<sub>1</sub><sub>NCCH<sub>3</sub></sub> does not fit the trend through the Cp<sub>d</sub> I series with anionic ligands. Corrections for RE<sub>Sub</sub> and RE<sub>Cpd I</sub> have no effect and keep the deviation for the acetonitrile reaction. It appears that the gas-phase results are only applicable to oxidants with the same total charge. We then tested whether single point calculations in a dielectric constant would solve the problems and calculated BDE<sub>OH</sub> values and barrier heights in a dielectric constant for the complete series of oxidants. As can be seen from Figure 8d, the solvent corrected BDE<sub>OH</sub> values correlate excellently with solvent corrected aromatic hydroxylation barrier heights for all reaction mechanisms that include overall neutral and cationic oxidants. Therefore, a comparison of Cp<sub>d</sub> I species with neutral versus anionic axial ligand systems will require solvent corrections to all energies, i.e. BDEs as well as barrier heights. Moreover, these studies show that the differences in reaction kinetics of neutral versus cationic oxidants is not due to the electronic properties of the oxidant but is purely a solvent effect, where the cationic species are stabilized strongly.

Recent studies of ours showed that reaction energies and barrier heights often correlate with a polarizability change for a reaction.<sup>55</sup> To find out whether that is also the case for the aromatic hydroxylation trends here, we calculated the polarizability trace from the Gaussian frequency calculations and converted this to a reaction polarizability ( $\Delta\alpha_r$ ) using eq 7. Thus, the polarizability trace in the barrier height is calculated from the individual polarizabilities of the transition state structure, Cp<sub>d</sub> I, and the substrate. In eq 7, these variables are given as  $\alpha_{\text{TS}}$ ,  $\alpha_{\text{Cpd I}}$ , and  $\alpha_{\text{SubH}}$ , respectively.

$$\Delta\alpha_r = \alpha_{\text{TS}} - \alpha_{\text{Cpd I}} - \alpha_{\text{SubH}} \quad (7)$$

Figure 9 displays the correlation between reaction polarizability ( $\Delta\alpha_r$ ) and barrier height for the aromatic hydroxylation barriers on low-spin states. The correlation is not perfect, but a trend is seen that gives a low polarizability change for systems

**Scheme 1. Thermodynamic Cycle Describing the Electron Transfer and Bond Formation Steps in the Electrophilic Addition Step in an Aromatic Hydroxylation Reaction by Cp<sub>d</sub> I(SH)**



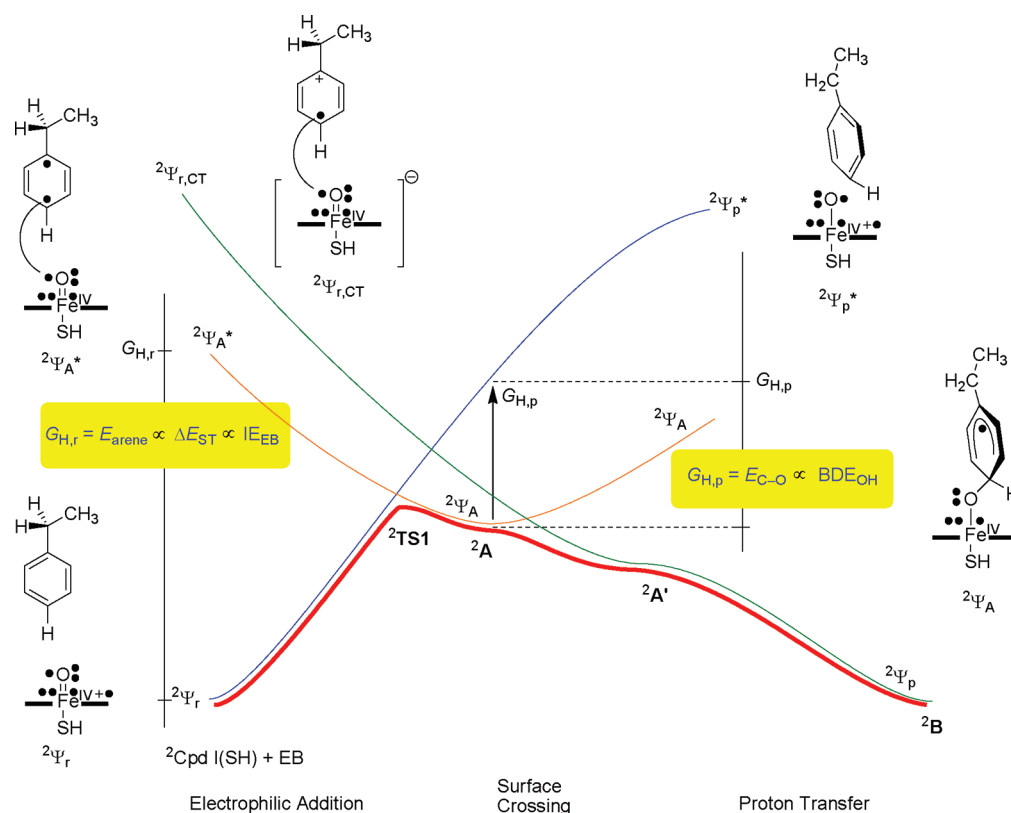


**Figure 10.** Valence bond curve crossing diagram for aromatic hydroxylation by  $^2\text{Cpd I}(\text{SH})$  via radical and cationic intermediates ( $^2\text{A}$ ,  $^2\text{A}'$ ) leading to the proton transfer intermediate  $^2\text{B}$ . The valence  $2\pi$  and  $3\pi^*$  orbitals are indicated with dots next to the Fe–O bond.

with low reaction barriers and a significantly larger barrier for systems that undergo a large change in polarizability.

Thus, the various thermodynamic correlations in Figures 8 and 9 show that the barrier height and consequently the rate constant of the aromatic hydroxylation reaction catalyzed by iron(IV)–oxo porphyrin cation radical oxidants is proportional to  $BDE_{OH}$  as well as to polarizability volume changes. So what is the origin of the correlation between barrier height and  $BDE_{OH}$  and why does the reaction pass a radical type  $\text{TS1}$  barrier? Previous studies<sup>26–28</sup> implicated mechanisms proceeding via a cationic intermediate, and hence our work seems to give a different reaction mechanism than that generally known.

In order to gain insight into the electron transfer processes in the initial stages of the reaction mechanism, we set up a thermodynamic cycle (Scheme 1) that explains the origins of electron and hydrogen atom transfer processes between ethylbenzene and Cpd I(SH). The scheme starts on the left with Cpd I(SH) and ethylbenzene (EB) as starting points and the reaction horizontal and to the right reflects the aromatic hydroxylation mechanism found above in Figure 5. An initial electrophilic addition step leads to the formation of a C–O bond and the transfer of one electron from the substrate into the half-filled  $a_{2u}$  orbital to give the radical complex  $^2\text{A}$ . This complex converts into the cationic intermediate  $^2\text{A}'$  via a second electron transfer from substrate to oxidant. We calculated all individual electron, proton, and hydrogen atom transfers involved in the overall reaction mechanism. Thus, an electron transfer in isolated reactions gives the one-electron reduced form of Cpd I and ionized ethylbenzene with an endothermicity of  $124.2 \text{ kcal mol}^{-1}$  due to an endothermic ionization potential of ethylbenzene of  $195.6 \text{ kcal mol}^{-1}$  and an

exothermic electron affinity of Cpd I of  $71.4 \text{ kcal mol}^{-1}$ . Solvent effects reduce the total electron transfer energy to  $45.1 \text{ kcal mol}^{-1}$  and additional thermal and entropic corrections give an electron transfer free energy of  $45.3 \text{ kcal mol}^{-1}$ . This large endothermicity for electron transfer, therefore, makes it unlikely that the reaction will be initiated by a single electron transfer.

To mimic the C–O bond formation step, we calculated the energy to add a hydrogen atom to both Cpd I(SH) and ethylbenzene to form  $^3[\text{Fe}^{\text{IV}}(\text{OH})(\text{Por})(\text{SH})]$  and  $^3[\text{EB} + \text{H}]$ . This reaction will distort the geometries of Cpd I and EB into geometries that apart from the C–O bond resemble those of intermediate complex A with the same electronic configuration and orbital occupation. The hydrogen abstraction enthalpy of Cpd I, of course, is equal to  $-BDE_{OH}$  by definition (eq 2). Both hydrogen atom abstraction processes are exothermic, namely, by  $88.9$  and  $23.1 \text{ kcal mol}^{-1}$ , respectively; hence, C–O bond formation should be the recommended process.

In a subsequent set of calculations, we calculate the electron affinity of  $^3[\text{Fe}^{\text{IV}}(\text{OH})(\text{Por})(\text{SH})]$  and the ionization potential of  $^2[\text{EB} + \text{H}]$ , which creates the two components that describe the cationic intermediate, namely,  $^4[\text{Fe}^{\text{III}}(\text{OH})(\text{Por})(\text{SH})]^-$  and  $^1[\text{EB} + \text{H}]^+$ . The reaction enthalpy is endothermic by a significant amount ( $+130.3 \text{ kcal mol}^{-1}$ ) mainly due to the large ionization potential of  $^2[\text{EB} + \text{H}]$ . Corrections due to solvent, thermal, and entropic contributions reduce the overall reaction enthalpy to  $49.0 \text{ kcal mol}^{-1}$ . On the basis of this thermochemical analysis, we predict the aromatic hydroxylation to proceed with an initial electrophilic addition step leading to a radical intermediate. The second electron transfer will take place later in the mechanism in the direction of the proton-transfer intermediate B.

Technically, there are two mechanisms from  ${}^2\text{A}$  to  ${}^2\text{B}$ : (1) directly via **TS2** and (2) through initial electron transfer from  ${}^2\text{A}$  to  ${}^2\text{A}'$  followed by relaxation toward  ${}^2\text{B}$ . The barrier ( ${}^2\text{TS2}$ ) leading to the proton transfer intermediate ( ${}^2\text{B}$ ) from  ${}^2\text{A}$  is relatively small ( $<1 \text{ kcal mol}^{-1}$ ) hence the electron transfer from  ${}^2\text{A}$  to  ${}^2\text{A}'$  may not be needed and  ${}^2\text{A}$  will collapse to  ${}^2\text{B}$  quickly and efficiently. Nevertheless, conversion of  ${}^2\text{A}$  to  ${}^2\text{A}'$  will also lead to  ${}^2\text{B}$  products, hence whether or not conversion from a radical to cationic intermediate in **A** happens or not, it will not affect the overall rate constants and product distributions.

Recent studies of Shaik and co-workers<sup>24</sup> on the aromatic oxidation by Cpd I(SH) explained the observed trends with a valence bond (VB) curve crossing diagram. These studies, however, used only one oxidant and a series of substrates. In this work we generalized the reactivity trends further by varying also the oxidant while keeping the same substrate. That way we can expand the VB diagram of Shaik et al. into the more general form as shown in Figure 10. This valence bond curve crossing diagram has analogies to those reported before for hydrogen atom transfer and double bond epoxidation reactions and most recently also shown for aromatic hydroxylation by Cpd I(SH).<sup>21–25,54,56</sup>

Figure 10 starts on the bottom left-hand-side with the reactant complexes  ${}^2\text{Cpd I(SH)}$  and ethylbenzene (EB), where Cpd I has the common  $2\pi_{xz}^2 2\pi_{yz}^2 3\pi_{xz}^{*1} 3\pi_{yz}^{*1} a_{2u}^1$  configuration with reactant wave function  ${}^2\Psi_r$ . The figure is virtually independent of the axial ligand bound to Cpd I, although the relative energies may vary. In a VB curve crossing diagram, the reactant wave function connects to an excited state in the product geometry  ${}^2\Psi_p^*$ . Thus,  ${}^2\Psi_p^*$  has the electronic configuration of the reactants but the geometry of the products, whereas  ${}^2\Psi_r$  has both reactant configuration and geometry. In our mechanism, however, the wave functions of reactant and products are crossed by several extra wave functions that represent the various intermediates along the reaction mechanism. The first of these is the radical intermediate ( ${}^2\text{A}$ ) that is described by the electronic configuration  $2\pi_{xz}^2 2\pi_{yz}^2 3\pi_{xz}^{*1} 3\pi_{yz}^{*1} a_{2u}^2 \pi_{Ar3}^{*1}$  and wave function  ${}^2\Psi_A$ , which connects to the excited state  ${}^2\Psi_A^*$  in the reactants geometry. The crossing of these two VB curves leads to an avoided crossing and a transition state for the electrophilic reaction mechanism ( ${}^2\text{TS1}$ ).

In VB theory, one can describe the barrier heights from physical properties of the reactants and/or products. Thus, it was shown that the barrier height ( $\Delta E^\ddagger$ ) that results from the crossing of two VB curves can be described (eq 8) as the difference of the curve crossing energy ( $\Delta E_c$ ) and the resonance energy  $B$ , so that the actual barrier is a factor  $B$  below the crossing point. It was further shown that the curve crossing energy is a fraction ( $f$ ) of the excitation energy from the reactant to the product wave function in the reactant geometry,  $G_{H,r}$ :

$$\Delta E^\ddagger = \Delta E_c - B = fG_{H,r} - B \quad (8)$$

In the case of aromatic hydroxylation leading to  ${}^2\text{A}$  intermediates, the barrier height, therefore, is proportional to the excitation from  ${}^2\Psi_r \rightarrow {}^2\Psi_A^*$ . The electron distributions of the VB structures on the left-hand-side of Figure 10 give the electronic differences between  ${}^2\Psi_r$  and  ${}^2\Psi_A^*$ , which determine  $G_{H,r}$ . For the electrophilic addition barrier leading to the radical intermediate, it follows that the height of **TS1**, therefore, is proportional to the excitation energy in the aromatic ring of the substrate ( $E_{\text{arene}}$ ). The latter is proportional to the singlet–triplet

energy ( $\Delta E_{\text{ST}}$ ) in that bond and, hence, the ionization energy of the substrate ( $IE_{\text{EB}}$ ). Indeed DFT calculated barrier heights of aromatic hydroxylation by Cpd I(SH) were found to correlate linearly with the ionization potential of the substrate.<sup>24</sup>

In this work we varied the oxidant and used a single substrate. Because of this difference, the VB modeling of the axial ligand effect calculations discussed here will represent the reverse reaction process and hence we should consider the barrier height starting in  ${}^2\text{A}$  in the direction of reactants. Equation 8 for the reverse reaction implies that the barrier height will be proportional to the excitation energy ( $G_{H,p}$ ) for the excitation from the radical wave function ( ${}^2\Psi_A$ ) to the reactant wave function in the geometry of the radical intermediate. As follows from the VB structure on the right-hand-side of Figure 10, the excitation  $G_{H,p}$  involves a singlet–triplet excitation in the C–O bond plus an electron transfer from substrate into  $a_{2u}$ . The C–O bond formation can be modeled via the use of  $BDE_{\text{OH}}$ ;<sup>29</sup> hence, the VB curve crossing diagram confirms the correlation between the electrophilic addition steps in aromatic hydroxylation with  $BDE_{\text{OH}}$ , as indeed observed before for a range of Cpd I species with varying axial ligands.

Finally, the VB curve crossing diagram also gives the charge-transfer VB curve that ultimately leads to the proton-transfer intermediate  ${}^2\text{B}$  and in reverse direction passes the cationic intermediate ( ${}^2\text{A}'$ ) and ends up as a high-lying excited state in the reactants with wave function  ${}^2\Psi_{r,CT}$ . In the reactants geometry, this state reflects the electron transfer state or the long-range complex between reduced Cpd I and ionized ethylbenzene,  $[\text{Fe}^{\text{IV}}(\text{O})(\text{Por})(\text{SH}) \cdots \text{EB}^+]$ . The wave function  ${}^2\Psi_{r,CT}$  crosses  ${}^2\Psi_A$  and converts the radical intermediate via the cationic intermediate into the proton transfer intermediate **B**. The Fe–O and O–C bond lengths of  ${}^2\text{A}$  are in between those found for  ${}^2\text{TS1}$  and  ${}^2\text{A}'$  (see Figure 5 above); therefore, it seems most likely that the surface crossing from  ${}^2\Psi_A$  to  ${}^2\Psi_{r,CT}$  takes place after  ${}^2\text{A}$  en route to the proton transfer intermediate. This is further supported by the charge and spin distributions of the various  ${}^2\text{TS1}$  and  ${}^2\text{A}$  structures, which are very similar (Supporting Information). Subsequently,  ${}^2\text{A}$  can either convert into  ${}^2\text{B}$  via the negligible barrier  ${}^2\text{TS2}$  directly or via a surface crossing to the saddle point  ${}^2\text{A}'$ , which also relaxes to  ${}^2\text{B}$ . Energetically there is very little difference between these two options and none affect the rate constant of the reaction. The exact position of the surface crossing will depend on the nature of the oxidant and the substrate. Thus, in the case of benzene hydroxylation by Cpd I(SH), we showed that the surface crossing appears early in the reaction mechanism, where the charge-transfer transition state was below the radical transition state.<sup>26a</sup> However, with ethylbenzene as a substrate, the surface crossing appears to take place later in the reaction mechanism. Earlier DFT studies on aromatic hydroxylation of ethylbenzene by heme and nonheme iron(IV)–oxo complexes also found C–O activation barriers with a large radical contribution on the substrate.<sup>26c,e,f</sup>

The correlation between barrier heights of electrophilic addition, such as aromatic hydroxylation, with  $BDE_{\text{OH}}$  will have consequences on regioselectivity reactions. Thus, recent work of ours<sup>22,29,54</sup> showed that the barrier heights for hydrogen atom abstraction, double bond epoxidation, and sulfoxidation reactions by Cpd I(X) models all are proportional to  $BDE_{\text{OH}}$ . This implies that the barrier heights, and consequently rate constants, of hydrogen atom abstraction, double bond epoxidation, sulfoxidation, and aromatic hydroxylation all correlate with  $BDE_{\text{OH}}$  and as a result their regioselectivities should not be dependent on



the oxidant but only on the substrate. These correlations further imply that the regioselectivity of a chemical reaction as catalyzed by enzymatic metal–oxo systems can only be varied through changes in the substrate binding pocket and not through chemical modifications of the oxidant itself.

## CONCLUSIONS

We have performed a systematic density functional theory study into the trans-influence of spectroscopic properties of Cpd I(X) species and the trans-effect on the kinetics and mechanism of aromatic hydroxylation reactions. Our studies show that the trans-influence is due to changes in the acidity of the oxidant due to the axial ligand. Surprisingly, the electronic effects appear to be lesser affected by the axial ligand and little changes in, for instance, the electron affinity of the oxidant is found. Furthermore, we investigated the aromatic hydroxylation of a model substrate (ethylbenzene) by these Cpd I(X) species. We show that the reaction barriers, and hence rate constants of the rate determining electrophilic addition step, are proportional to  $BDE_{OH}$ . These results enable one to predict barrier heights of aromatic hydroxylation reactions empirically. The reactivity patterns are rationalized with thermochemical cycles and a valence bond curve crossing diagram, which explain the mechanism observed and also give evidence to the reason behind the correlation of barrier height with  $BDE_{OH}$ . Thus, the reaction proceeds via a radical intermediate, which can interconvert into a cationic intermediate. The latter is a saddle point en route to the proton-transfer intermediate that is the precursor to the phenol product complex. We also show, for the first time, that trends through series of anionic and neutral axial ligands are linear when solvent corrected energies and BDEs are used, which enabled us to generalize reactivity patterns further. Consequently, the reactivity differences between neutral and cationic oxidants are solvent dependent and do not originate from electronic differences.

## ASSOCIATED CONTENT

**S Supporting Information.** Detailed supporting information including group spin densities, charges, and absolute and relative energies of all structures described in this work as well as Cartesian coordinates of all optimized geometries, and references 31b and 31c. This material is available free of charge via the Internet at <http://pubs.acs.org>.

## AUTHOR INFORMATION

### Corresponding Author

\*E-mail: [sam.devisser@manchester.ac.uk](mailto:sam.devisser@manchester.ac.uk) (S.P.d.V.); [dkclcre@yahoo.com](mailto:dkclcre@yahoo.com) (D.K.).

## ACKNOWLEDGMENT

The authors thank the National Service for Computational Chemistry Software (NSCCS) for CPU time. D.K. holds a Ramanujan Fellowship from the Department of Science and Technology (DST), New Delhi (India), and acknowledges its financial support (Research Grants SR/S2/RJN-11/2008 and SR/S1/PC-58/2009).

## REFERENCES

- (1) (a) Guengerich, F. P. *Chem. Res. Toxicol.* **2001**, *14*, 611–650. (b) Munro, A. W.; Girvan, H. M.; McLean, K. J. *Nat. Prod. Rep.* **2007**, *24*, 585–609.
- (2) (a) Sono, M.; Roach, M. P.; Coulter, E. D.; Dawson, J. H. *Chem. Rev.* **1996**, *96*, 2841–2888. (b) Groves, J. T. *Proc. Natl. Acad. Sci. U.S.A.* **2003**, *100*, 3569–3574. (c) Ortiz de Montellano, P. R., Ed.; *Cytochrome P450: Structure, Mechanism and Biochemistry*, 3rd ed.; Kluwer Academic/Plenum Publishers: New York, 2004. (d) Kadish, K. M., Smith, K. M., Guillard, R., Eds. *Handbook of Porphyrin Science*; World Scientific Publishing Co.: Singapore, 2010. (e) Ortiz de Montellano, P. R. *Chem. Rev.* **2010**, *110*, 932–948. (f) de Visser, S. P.; Kumar, D., Eds. *Iron-Containing Enzymes: Versatile Catalysts of Hydroxylation Reaction in Nature*; RSC Publishing: Cambridge, U.K., 2011.
- (3) O'Reilly, E.; Köhler, V.; Flitch, S. L.; Turner, N. J. *Chem. Commun.* **2010**, *47*, 2490–2501.
- (4) (a) Sarabia, S. F.; Zhu, B. T.; Kurosawa, T.; Tohma, M.; Liehr, J. G. *Chem. Res. Toxicol.* **1997**, *10*, 767–771. (b) Huang, Z.; Guengerich, F. P.; Kaminsky, L. S. *Carcinogenesis* **1998**, *19*, 867–872. (c) Lee, A. J.; Cai, M. X.; Thomas, P. E.; Conney, A. H.; Zhu, B. T. *Endocrinology* **2003**, *144*, 3382–3398.
- (5) Guo, J.; Liu, D.; Nikolic, D.; Pezzuto, J. M.; Van Breemen, R. B. *Drug Metab. Dispos.* **2008**, *36*, 461–468.
- (6) (a) Jonsson, J. *Acta Pharmacol. Toxicol.* **1977**, *40*, 517–528. (b) Carvalho, F.; Soares, M. E.; Fernandes, E.; Remião, F.; Carvalho, M.; Duarte, J. A.; Pires-das-Neves, R.; De Lourdes Pereira, M.; De Lourdes Bastos, M. J. *Health Sci.* **2007**, *53*, 371–377. (c) Hu, Y.; Dehal, S. S.; Hynd, G.; Jones, G. B.; Kupfer, D. *Xenobiotica* **2003**, *33*, 141–151.
- (7) Narimatsu, S.; Tachibana, M.; Masubuchi, Y.; Imaoka, S.; Funae, Y.; Suzuki, T. *Biol. Pharm. Bull.* **1995**, *18*, 1060–1065.
- (8) Herraiz, T.; Guillén, H.; Arán, V. J.; Idle, J. R.; Gonzalez, F. J. *Toxicol. Appl. Pharmacol.* **2006**, *216*, 387–398.
- (9) Potter, G. A.; Patterson, L. H.; Wanogho, E.; Perry, P. J.; Butler, P. C.; Ijaz, T.; Ruparelia, K. C.; Lamb, J. H.; Farmer, P. B.; Stanley, L. A.; Burke, M. D. *Br. J. Cancer* **2002**, *86*, 774–778.
- (10) Pfister, T. D.; Ohki, T.; Ueno, T.; Hara, I.; Adachi, S.; Makino, Y.; Ueyama, N.; Lu, Y.; Watanabe, Y. *J. Biol. Chem.* **2005**, *280*, 12858–12866.
- (11) (a) Denisov, I. G.; Makris, T. M.; Sligar, S. G.; Schlichting, I. *Chem. Rev.* **2005**, *105*, 2253–2277. (b) Watanabe, Y.; Nakajima, H.; Ueno, T. *Acc. Chem. Res.* **2007**, *40*, 554–562. (c) Nam, W. *Acc. Chem. Res.* **2007**, *40*, 522–531.
- (12) (a) Groves, J. T.; Shalyaev, K.; Lee, J. In *The Porphyrin Handbook*; Kadish, K. M., Smith, K. M., Guillard, R., Eds.; Academic Press: New York, 2000; Vol. 4, Chapter 27, pp 17–40. (b) Shaik, S.; Hirao, H.; Kumar, D. *Acc. Chem. Res.* **2007**, *40*, 532–542.
- (13) (a) Egawa, T.; Shimada, H.; Ishimura, Y. *Biochem. Biophys. Res. Commun.* **1994**, *201*, 1464–1469. (b) Kellner, D. G.; Hung, S. C.; Weiss, K. E.; Sligar, S. G. *J. Biol. Chem.* **2002**, *277*, 9641–9644. (c) Hessenauer-Ilicheva, N.; Franke, A.; Meyer, D.; Woggon, W.-D.; van Eldik, R. J. *Am. Chem. Soc.* **2007**, *129*, 12473–12479. (d) Chiavarino, B.; Cipollini, R.; Crestoni, M. E.; Fornarini, S.; Lanucara, F.; Lapi, A. *J. Am. Chem. Soc.* **2008**, *130*, 3208–3217.
- (14) (a) Green, M. T. *J. Am. Chem. Soc.* **1999**, *121*, 7939–7940. (b) Ogliaro, F.; de Visser, S. P.; Cohen, S.; Kaneti, J.; Shaik, S. *ChemBioChem* **2001**, *11*, 848–851.
- (15) Rittle, J.; Green, M. T. *Science* **2010**, *330*, 933–937.
- (16) (a) Poulos, T. L.; Finzel, B. C.; Howard, A. J. *J. Mol. Biol.* **1987**, *195*, 687–700. (b) Raag, R.; Poulos, T. L. *Biochemistry* **1989**, *28*, 7586–7592. (c) Green, M. T.; Dawson, J. H.; Gray, H. B. *Science* **2004**, *304*, 1653–1656. (d) Schlichting, I.; Berendzen, J.; Chu, K.; Stock, A. M.; Maves, S. A.; Benson, D. E.; Sweet, R. M.; Ringe, D.; Petsko, G. A.; Sligar, S. G. *Science* **2000**, *287*, 1615–1622.
- (17) (a) Dunford, H. B. *Heme Peroxidases*; Wiley-VCH: New York, 1999. (b) Poulos, T. L. *Peroxidases and Cytochrome P450*. In *The Porphyrin Handbook*; Kadish, K. M., Smith, K. M., Guillard, R., Eds.; Academic Press: San Diego, CA, 2000; Vol. 4, Chapter 32, pp 189–218. (c) Veitch, N. C.; Smith, A. T. *Adv. Inorg. Chem.* **2000**, *51*, 107–162.

- (d) Gajhede, M. *The Handbook of Metalloproteins*; Messerschmidt, A., Huber, R., Poulos, T. L., Wieghardt, K., Eds.; Wiley: New York, 2001; Vol. 1, pp 195–210.
- (18) Dawson, J. H.; Holm, R. H.; Trudell, J. R.; Barth, G.; Linder, R. E.; Bunnenberg, E.; Djerassi, C.; Tang, S. C. *J. Am. Chem. Soc.* **1976**, *98*, 3707–3709.
- (19) (a) Gross, Z.; Nimri, S. *Inorg. Chem.* **1994**, *33*, 1731–1732. (b) Gross, Z. *J. Biol. Inorg. Chem.* **1996**, *1*, 368–371. (c) Czarnecki, K.; Nimri, S.; Gross, Z.; Proniewicz, L. M.; Kincaid, J. R. *J. Am. Chem. Soc.* **1996**, *118*, 2929–2935.
- (20) (a) Sastri, C. V.; Park, M. J.; Ohta, T.; Jackson, T. A.; Stubna, A.; Seo, M. S.; Lee, J.; Kim, J.; Kitagawa, T.; Münck, E.; et al. *J. Am. Chem. Soc.* **2005**, *127*, 12494–12495. (b) Song, W. J.; Ryu, Y. O.; Song, R.; Nam, W. *J. Biol. Inorg. Chem.* **2005**, *10*, 294–304. (c) Sastri, C. V.; Lee, J.; Oh, K.; Lee, Y. J.; Lee, J.; Jackson, T. A.; Ray, K.; Hirao, H.; Shin, W.; Halfen, J. A.; Nam, W.; et al. *Proc. Natl. Acad. Sci. U.S.A.* **2007**, *104*, 19181–19186. (d) Hirao, H.; Que, L., Jr.; Nam, W.; Shaik, S. *Chem.—Eur. J.* **2008**, *14*, 1740–1756. (e) Jackson, T. A.; Rohde, J.-U.; Seo, M. S.; Sastri, C. V.; DeHont, R.; Stubna, A.; Ohta, T.; Kitagawa, T.; Münck, E.; Nam, W.; Que, L., Jr. *J. Am. Chem. Soc.* **2008**, *130*, 12394–12407. (f) Fukuzumi, S.; Kotani, H.; Suenobu, T.; Hong, S.; Lee, Y.-M.; Nam, W. *Chem.—Eur. J.* **2009**, *15*, 354–361. (g) Kang, Y.; Chen, H.; Jeong, Y. J.; Lai, W.; Bae, E. H.; Shaik, S.; Nam, W. *Chem.—Eur. J.* **2009**, *15*, 10039–10046.
- (21) (a) Shaik, S.; Kumar, D.; de Visser, S. P. *J. Am. Chem. Soc.* **2008**, *130*, 10128–10140. (b) Shaik, S.; Lai, W.; Chen, H.; Wang, Y. *Acc. Chem. Res.* **2010**, *43*, 1154–1165.
- (22) Kumar, D.; Karamzadeh, B.; Sastry, G. N.; de Visser, S. P. *J. Am. Chem. Soc.* **2010**, *132*, 7656–7667.
- (23) Shaik, S.; Wang, Y.; Chen, H.; Song, J.; Meir, R. *Faraday Discuss.* **2010**, *145*, 49–70.
- (24) Shaik, S.; Milko, P.; Schyman, P.; Usharani, D.; Chen, H. *J. Chem. Theory Comput.* **2011**, *7*, 327–339.
- (25) (a) Jones, J. P.; Mysinger, M.; Korzekwa, K. R. *Drug Metab. Dispos.* **2002**, *30*, 7–12. (b) Dowers, T. S.; Rock, D. A.; Rock, D. A.; Perkins, B. N. S.; Jones, J. P. *Drug Metab. Dispos.* **2004**, *32*, 328–332. (c) Dowers, T. S.; Jones, J. P. *Drug Metab. Dispos.* **2006**, *34*, 1288–1290.
- (26) (a) de Visser, S. P.; Shaik, S. *J. Am. Chem. Soc.* **2003**, *125*, 7413–7424. (b) Kumar, D.; de Visser, S. P.; Shaik, S. *Chem.—Eur. J.* **2005**, *11*, 2825–2835. (c) de Visser, S. P. *Chem.—Eur. J.* **2006**, *12*, 8168–8177. (d) Hazan, C.; Kumar, D.; de Visser, S. P.; Shaik, S. *Eur. J. Inorg. Chem.* **2007**, 2966–2974. (e) de Visser, S. P.; Tahsini, L.; Nam, W. *Chem.—Eur. J.* **2009**, *15*, 5577–5587. (f) de Visser, S. P.; Latifi, R.; Tahsini, L.; Nam, W. *Chem. Asian J.* **2011**, *6*, 493–504.
- (27) (a) Bathelt, C. M.; Ridder, L.; Mulholland, A. J.; Harvey, J. N. *J. Am. Chem. Soc.* **2003**, *125*, 15004–15005. (b) Bathelt, C. M.; Ridder, L.; Mulholland, A. J.; Harvey, J. N. *Org. Biomol. Chem.* **2004**, *2*, 2998–3005. (c) Bathelt, C. M.; Mulholland, A. J.; Harvey, J. N. *J. Phys. Chem. A* **2008**, *112*, 13149–13156.
- (28) Rydberg, P.; Ryde, U.; Olsen, L. *J. Phys. Chem. A* **2008**, *112*, 13058–13065.
- (29) de Visser, S. P. *J. Am. Chem. Soc.* **2010**, *132*, 1087–1097.
- (30) (a) Li, C.; Wu, W.; Kumar, D.; Shaik, S. *J. Am. Chem. Soc.* **2006**, *128*, 394–395. (b) Kumar, D.; Thiel, W.; de Visser, S. P. *J. Am. Chem. Soc.* **2011**, *133*, 3869–3882.
- (31) (a) *Jaguar*, version 7.7; Schrödinger, LLC: New York, 2010. (b) Frisch, M. J. et al. *Gaussian 03*, revision C.01; Gaussian, Inc.: Wallingford, CT, 2004. (c) Frisch, M. J. et al. *Gaussian 09*; Gaussian, Inc.: Wallingford, CT, 2009.
- (32) (a) Becke, A. D. *J. Chem. Phys.* **1993**, *98*, 5648–5652. (b) Lee, C.; Yang, W.; Parr, R. G. *Phys. Rev. B* **1988**, *37*, 785–789.
- (33) (a) Hay, P. J.; Wadt, W. R. *J. Chem. Phys.* **1985**, *82*, 270–283. (b) Hehre, W. J.; Ditchfield, R.; Pople, J. A. *J. Chem. Phys.* **1972**, *56*, 2257–2261.
- (34) Scott, A. P.; Radom, L. *J. Phys. Chem.* **1996**, *100*, 16502–16513.
- (35) (a) Derat, E.; Kumar, D.; Hirao, H.; Shaik, S. *J. Am. Chem. Soc.* **2006**, *128*, 473–484. (b) de Visser, S. P.; Oh, K.; Han, A.-R.; Nam, W. *Inorg. Chem.* **2007**, *46*, 4632–4641.
- (36) (a) Heyes, D. J.; Sakuma, M.; de Visser, S. P.; Scrutton, N. S. *J. Biol. Chem.* **2009**, *284*, 3762–3767. (b) Porro, C. S.; Kumar, D.; de Visser, S. P. *Phys. Chem. Chem. Phys.* **2009**, *11*, 10219–10226. (c) Karamzadeh, B.; Kumar, D.; Sastry, G. N.; de Visser, S. P. *J. Phys. Chem. A* **2010**, *114*, 13234–13243.
- (37) (a) Handy, N. C.; Cohen, A. J. *Mol. Phys.* **2001**, *99*, 403–412. (b) Hoe, W.-M.; Cohen, A.; Handy, N. C. *Chem. Phys. Lett.* **2001**, *341*, 319–328. (c) Perdew, J. P.; Burke, K.; Ernzerhof, M. *Phys. Rev. Lett.* **1996**, *77*, 3865–3868.
- (38) Reiher, M.; Salomon, O.; Hess, B. A. *Theor. Chem. Acc.* **2001**, *107*, 48–55.
- (39) Kumar, D.; Tahsini, L.; de Visser, S. P.; Kang, H. Y.; Kim, S. J.; Nam, W. *J. Phys. Chem. A* **2009**, *113*, 11713–11722.
- (40) Shaik, S.; Kumar, D.; de Visser, S. P.; Altun, A.; Thiel, W. *Chem. Rev.* **2005**, *105*, 2279–2328.
- (41) de Visser, S. P.; Shaik, S.; Sharma, P. K.; Kumar, D.; Thiel, W. *J. Am. Chem. Soc.* **2003**, *125*, 15779–15788.
- (42) (a) Poulos, T. L. *J. Biol. Inorg. Chem.* **1996**, *1*, 356–359. (b) Sigman, J. A.; Pond, A. E.; Dawson, J. H.; Lu, Y. *Biochemistry* **1999**, *38*, 11122–11129. (c) Suzuki, N.; Higuchi, T.; Urano, Y.; Kikuchi, K.; Uekusa, H.; Ohashi, Y.; Uchida, T.; Kitagawa, T.; Nagano, T. *J. Am. Chem. Soc.* **1999**, *121*, 11571–11572.
- (43) Badger, R. M. *J. Chem. Phys.* **1935**, *3*, 710–714.
- (44) Green, M. T. *J. Am. Chem. Soc.* **2006**, *128*, 1902–1906.
- (45) (a) Schöneboom, J. C.; Lin, H.; Reuter, N.; Thiel, W.; Cohen, S.; Ogliaro, F.; Shaik, S. *J. Am. Chem. Soc.* **2002**, *124*, 8142–8151. (b) Bathelt, C. M.; Zurek, J.; Mulholland, A. J.; Harvey, J. N. *J. Am. Chem. Soc.* **2005**, *127*, 12900–12908.
- (46) Siegbahn, P. E. M.; Borowski, T. *Acc. Chem. Res.* **2006**, *39*, 729–736.
- (47) (a) Friedrich, L. E. *J. Org. Chem.* **1983**, *48*, 3851–3852. (b) Bordwell, F. G.; Cheng, J.-P. *J. Am. Chem. Soc.* **1991**, *113*, 1736–1743. (c) Bordwell, F. G.; Cheng, J.-P.; Ji, G.-Z.; Satish, A. V.; Zhang, X. *J. Am. Chem. Soc.* **1991**, *113*, 9790–9795.
- (48) (a) Prokop, K. A.; de Visser, S. P.; Goldberg, D. P. *Angew. Chem., Int. Ed.* **2010**, *49*, 5091–5095. (b) Prokop, K. A.; Neu, H. M.; de Visser, S. P.; Goldberg, D. P. *J. Am. Chem. Soc.* **2011**, *133*, 15874–15877.
- (49) Proshlyakov, D. A.; Henshaw, T. F.; Monterosso, G. R.; Ryle, M. J.; Hausinger, R. P. *J. Am. Chem. Soc.* **2004**, *126*, 1022–1023.
- (50) Bassan, A.; Blomberg, M. R. A.; Siegbahn, P. E. M. *Chem.—Eur. J.* **2003**, *9*, 4055–4067.
- (51) (a) Rydberg, P.; Sigfridsson, E.; Ryde, U. *J. Biol. Inorg. Chem.* **2004**, *9*, 203–223. (b) Kumar, D.; de Visser, S. P.; Sharma, P. K.; Derat, E.; Shaik, S. *J. Biol. Inorg. Chem.* **2005**, *10*, 181–189. (c) de Visser, S. P. *J. Biol. Inorg. Chem.* **2006**, *11*, 168–178. (d) de Visser, S. P. *J. Phys. Chem. B* **2006**, *110*, 20759–20761. (e) Wang, R.; de Visser, S. P. *J. Inorg. Biochem.* **2007**, *101*, 1464–1472.
- (52) (a) Mayer, J. M. *Acc. Chem. Res.* **1998**, *31*, 441–450. (b) Mayer, J. M. *Annu. Rev. Phys. Chem.* **2004**, *55*, 363–390. (c) Mader, E. A.; Manner, V. W.; Markle, T. F.; Wu, A.; Franz, J. A.; Mayer, J. M. *J. Am. Chem. Soc.* **2009**, *131*, 4335–4345. (d) Kaizer, J.; Klinker, E. J.; Oh, N. Y.; Rohde, J.-U.; Song, W. J.; Stubna, A.; Kim, J.; Münck, E.; Nam, W.; Que, L., Jr. *J. Am. Chem. Soc.* **2004**, *126*, 472–473. (e) Yoon, J.; Wilson, S. A.; Jang, Y. K.; Seo, M. S.; Nehru, K.; Hedman, B.; Hodgson, K. O.; Bill, E.; Solomon, E. I.; Nam, W. *Angew. Chem., Int. Ed.* **2009**, *48*, 1257–1260. (f) Lansky, D. E.; Goldberg, D. P. *Inorg. Chem.* **2006**, *45*, 5119–5125. (g) Bell, S. R.; Groves, J. T. *J. Am. Chem. Soc.* **2009**, *131*, 9640–9641.
- (53) (a) de Visser, S. P.; Kumar, D.; Cohen, S.; Shacham, R.; Shaik, S. *J. Am. Chem. Soc.* **2004**, *126*, 8362–8363. (b) Latifi, R.; Bagherzadeh, M.; de Visser, S. P. *Chem.—Eur. J.* **2009**, *15*, 6651–6662.
- (54) Kumar, D.; Sastry, G. N.; de Visser, S. P. *Chem.—Eur. J.* **2011**, *17*, 6196–6205.
- (55) (a) de Visser, S. P. *Phys. Chem. Chem. Phys.* **1999**, *1*, 749–753. (b) de Visser, S. P. *J. Phys. Chem. B* **2011**, *115*, 4709–4717. (c) de Visser, S. P. *Chem. Phys. Lett.* **2011**, *515*, 170–172.
- (56) Shaik, S. *Phys. Chem. Chem. Phys.* **2010**, *12*, 8706–8720.